

## Supporting Information

### **Porous, *n-p*Type Ultra-long, ZnO@Bi<sub>2</sub>O<sub>3</sub> Heterojunction Nanorods based NO<sub>2</sub> Gas Sensor: New insights towards Charge Transport Characteristics**

Vishnuraj Ramakrishnan<sup>a</sup>, Keerthi G Nair<sup>a</sup>, Jayaseelan Dhakshinamoorthy<sup>a</sup>, K.R.Ravi<sup>b</sup> and Biji Pullithadathil<sup>a,\*</sup>

---

\*Corresponding author Email: [bijuja123@yahoo.co.in](mailto:bijuja123@yahoo.co.in); [pbm@psqias.ac.in](mailto:pbm@psqias.ac.in)

#### **1. Synthesis of porous ultra-long ZnO nanorods:**

Porous ultra-long ZnO nanorods were synthesized using simple one-pot hydrothermal method. Briefly, 0.02 M of zinc chloride, 0.06 M of SDS and 1.4 M of Na<sub>2</sub>CO<sub>3</sub> were consecutively added to 80 mL of ultrapure water (Merck-Millipore, resistivity: 18.2 MΩ-cm) and continue stirring at room temperature to obtain a milky white dispersion. After 5 h of stirring, this mixture was transferred to a Teflon-lined stainless steel autoclave and volume was made up to 90% using ultrapure water. The dispersed solution was further treated with hydrothermal process for 12 h at 140°C. After the completion of reaction, autoclave was cooled down to room temperature and precipitate was separated, washed and centrifuged several times using mixture of ultrapure water and ethanol. Finally, the purified material was vacuum dried at 90°C for 12h. As synthesized powder samples was annealed at 500°C for 2 h and taken for further characterizations.

#### **2. Synthesis of ultra-long Bi<sub>2</sub>O<sub>3</sub> nanorods:**

The pure Bi<sub>2</sub>O<sub>3</sub> ultra-long nanorods were synthesized by the co-precipitation method. In this typical procedure, 50 ml (0.05 M) bismuth nitrate solution is prepared using deionized water and kept constant stirring at 80°C. To this above solution 50 ml (5 M) NaOH solution was added drop by drop. The change of colour from white to yellow was observed which confirms the formation of α-Bi<sub>2</sub>O<sub>3</sub> nanorods and stirring has been continuous for 1 h. The yellow precipitate is washed with ethanol and distilled water for several times and dried at 60°C for 6 h in a hot air oven.

### 3. Optical Characterization:

Solid state UV–visible diffuses reflectance spectra (DRS) of ZnO nanorods and ZnO@Bi<sub>2</sub>O<sub>3</sub> heterojunction nanorods shown in Figure S1. ZnO nanorods exhibits UV absorption peak centered at 365nm, which corresponds to the ground excitonic peak of Zn-O. Also ZnO@Bi<sub>2</sub>O<sub>3</sub> nanorods exhibit the same with an additional broad peak near the region of 450nm. The crystalline purity of the sample has been confirmed by observing absence of additional peaks in the spectrum.

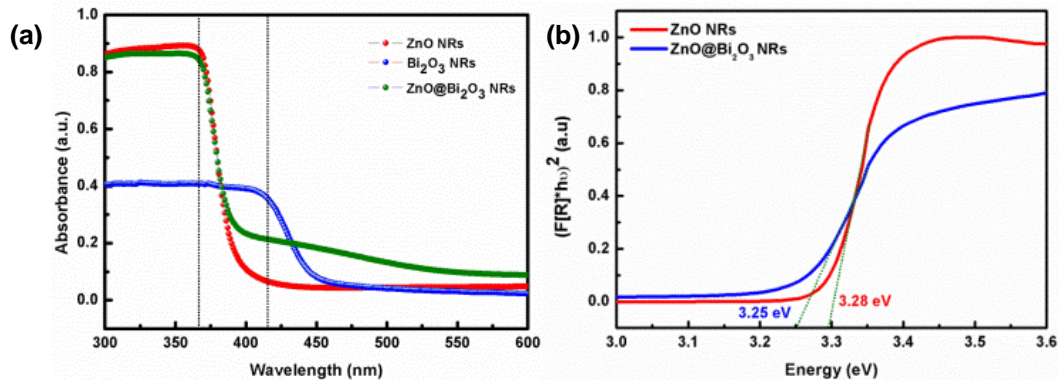


**Figure S1(a)** UV–vis DRS spectra of ultra-long ZnO nanorods and ZnO@Bi<sub>2</sub>O<sub>3</sub> heterojunction nanorods. **(b)** Kubelka-Munk function versus energy plots of ultra-long ZnO nanorods and ZnO@Bi<sub>2</sub>O<sub>3</sub> heterojunction nanorods.

The band gap energy of the samples is measured by the extrapolation of the linear portion of the graph between the modified Kubelka-Munk function  $[F(R) \cdot h\nu]^2$  versus photon energy ( $h\nu$ ) shown in the inset figure S1 (b).

$$F_{KM} = \frac{(1-R)^2}{2R} \quad (\text{eq 1})$$

The band gaps of the pristine ZnO nanorods and heterojunction ZnO@Bi<sub>2</sub>O<sub>3</sub> nanorods were calculated to be 3.26 and 3.21 eV respectively. The considerable change observed in the band gaps is due to the interfacial electron transfer between ZnO nanorods and Bi<sub>2</sub>O<sub>3</sub> nanoclusters as shell layer.

Room temperature photo-luminescence (RTPL) spectra of ultra-long ZnO nanorods and ZnO@Bi<sub>2</sub>O<sub>3</sub> heterojunction nanorods are shown in Fig.S2. The predominant emission peak

observed in the UV region (380 nm) at 3.17 eV corresponds to the free exciton emission of Zn-O. ZnO possess large exciton binding energy (60 meV) and exhibit PL emission due to the donor bound exciton and free exciton. As small and significant shift was observed for ultra-long ZnO@Bi<sub>2</sub>O<sub>3</sub> heterojunctions with decreased emission peak intensity, indicating the charge transfer process between conduction band of ZnO to conduction band of Bi<sub>2</sub>O<sub>3</sub>. Corresponding band diagram shown in the Figure S2 explains, due to the electron transfer process, the electron density on the surface of Bi<sub>2</sub>O<sub>3</sub> nanoclusters increases leading to the formation of depletion layer at the junctions. Since Bi<sub>2</sub>O<sub>3</sub> nanoparticles on the surface of ZnO nanorods can extract electrons from the conduction band, both direct and trap related charge carrier recombination pathways are blocked. Due to the interaction between ZnO and Bi<sub>2</sub>O<sub>3</sub> at the interfacial heterojunctions, a high electron density could be created on ZnO@Bi<sub>2</sub>O<sub>3</sub> surface. This accumulation of charge density further triggers the formation of highly energetic plasmons which along with energetic electrons promotes the electron transfer phenomenon. In comparison with bare ultra-long nanorods, the ZnO@Bi<sub>2</sub>O<sub>3</sub> heterojunction nanorod's electron acceptor level (AL) and donor level differs due to the utilization of defects during the surface growth of Bi<sub>2</sub>O<sub>3</sub> nanoparticles.

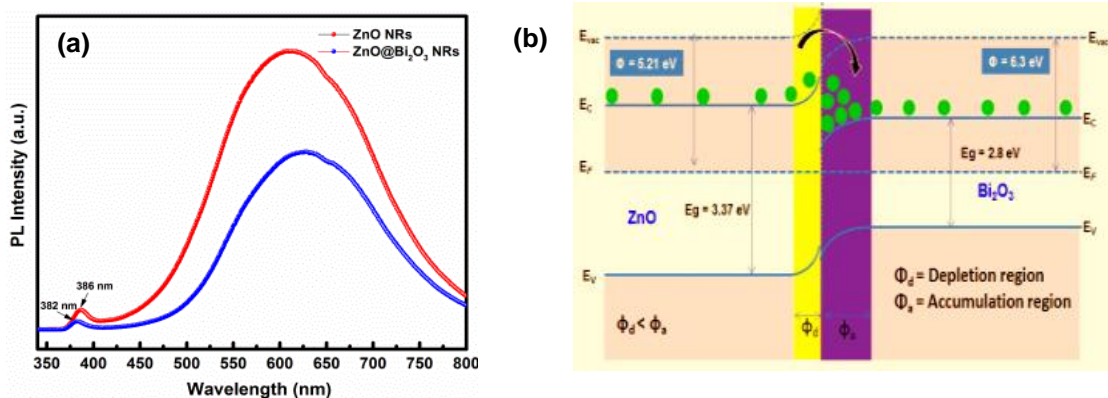


**Figure S2** (a) RTPL spectra of pristine ultra-long ZnO nanorods and ZnO@ Bi<sub>2</sub>O<sub>3</sub> heterojunction nanorods. (b) Band diagram showing the electron transfer at the heterojunctions.

#### 4. Morphological Analysis:

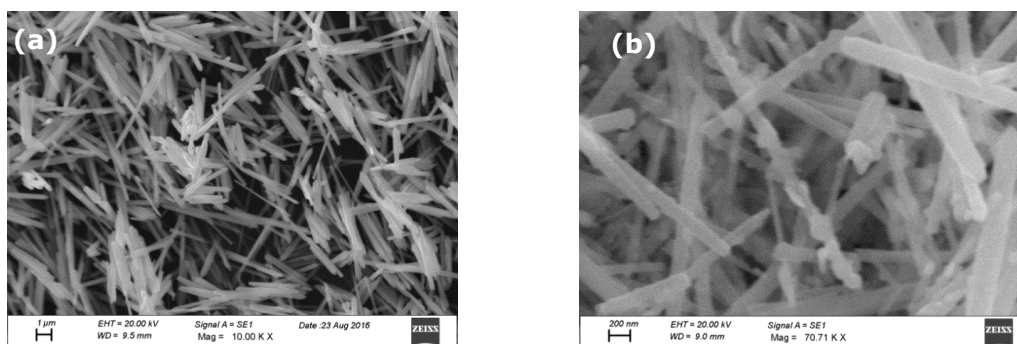
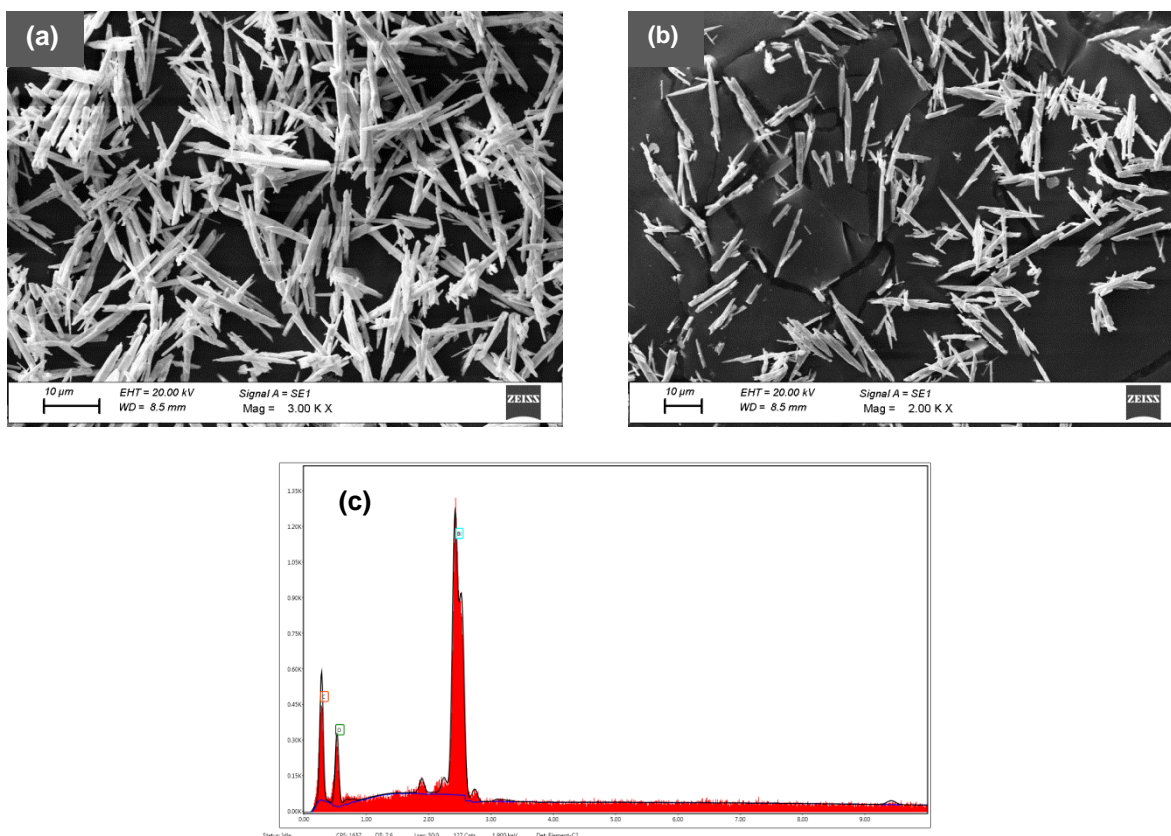


**Figure S3.** SEM images of (a) Ultra-long ZnO nanorods and (b) Ultra-long ZnO@Bi<sub>2</sub>O<sub>3</sub> heterojunction nanorods.

Figure S3 (a-b) shows the typical SEM images of as-obtained ultra-long ZnO nanorods and ZnO@Bi<sub>2</sub>O<sub>3</sub> heterojunction nanorods were grown by hydrothermal/solvothermal process. The image shows the surface of the ZnO NRs were smooth and homogeneous dimension. The average length of the ZnO nanorods were  $15\mu\text{m} \pm 0.5\mu\text{m}$  and the width of ZnO nanorods was about  $150\text{ nm} \pm 0.3\text{nm}$ . Figure S3 (b) confirms that the Bi<sub>2</sub>O<sub>3</sub> nanoclusters were attached on the surface boundary of the ZnO nanorods forming the heterojunction structures.

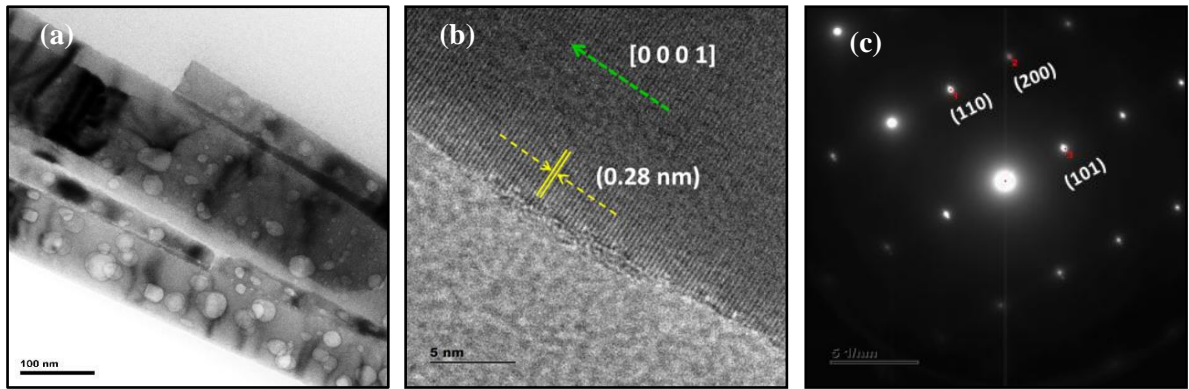
#### 5. SEM Images of ultralong Bi<sub>2</sub>O<sub>3</sub> nanorods:

The typical SEM images of ultra long Bi<sub>2</sub>O<sub>3</sub> nanorods are shown in Figure S4 (a-c) grown by hydrothermal process. The image shows the surface of the Bi<sub>2</sub>O<sub>3</sub> nanorods were smooth and homogeneous dimension. The average length of the ultra long Bi<sub>2</sub>O<sub>3</sub> nanorods were  $14\mu\text{m} \pm 0.5\mu\text{m}$  and the width of Bi<sub>2</sub>O<sub>3</sub> nanorods was about  $900\text{ nm} \pm 10\text{ nm}$ . The corresponding EDS are shown in Figure S4(c) for ultra long Bi<sub>2</sub>O<sub>3</sub> nanorods.



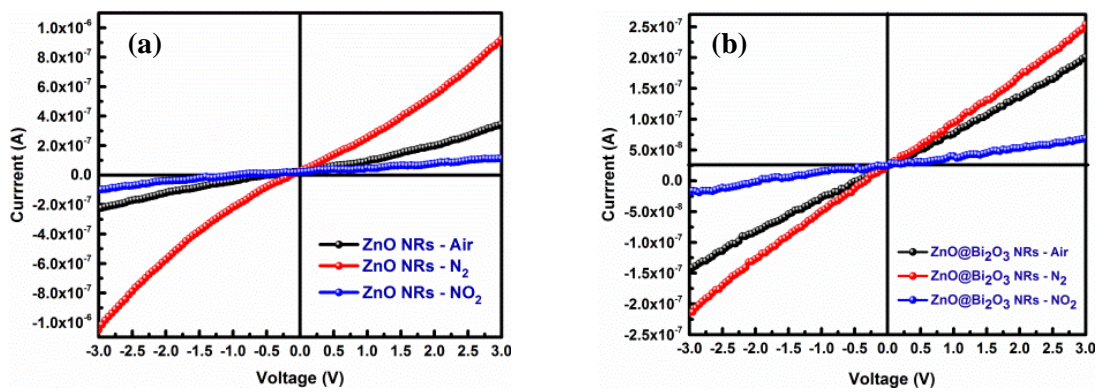
**Figure S4.** (a-b) SEM images of Ultra-long  $\text{Bi}_2\text{O}_3$  nanorods (c) corresponding EDX spectrum.

TEM analysis was carried out for ultra-long ZnO nanorods to infer about the structure and morphological characteristics. Fig. S5(a) shows the TEM images of bare ultra-long ZnO nanorods, where the uniform distribution of nanorods having length and width of  $15 \pm 0.5 \mu\text{m}$  and  $150 \pm 0.5 \text{ nm}$  respectively were observed. Each ultra-long nanorod extends to several micrometers with high aspect ratio as suited for electronics and sensing applications. Inset showing HR-TEM image of ZnO nanorods clearly shows the d-spacing value of 0.25 nm between the adjacent lattice planes corresponding to (100) plane lattice distance of hexagonal-wurtzite structured ZnO, indicating the growth direction along *c*-axis [0001]. Fig. S5 (b) shows the magnified image of ZnO nanorod and inset showing the SAED pattern of ultra-long ZnO nanorods clearly implies the growth direction of ZnO in *c*-axis with single crystalline nature. The SAED pattern were indexed and matching with the standard JCPDS data card no.65-3411.

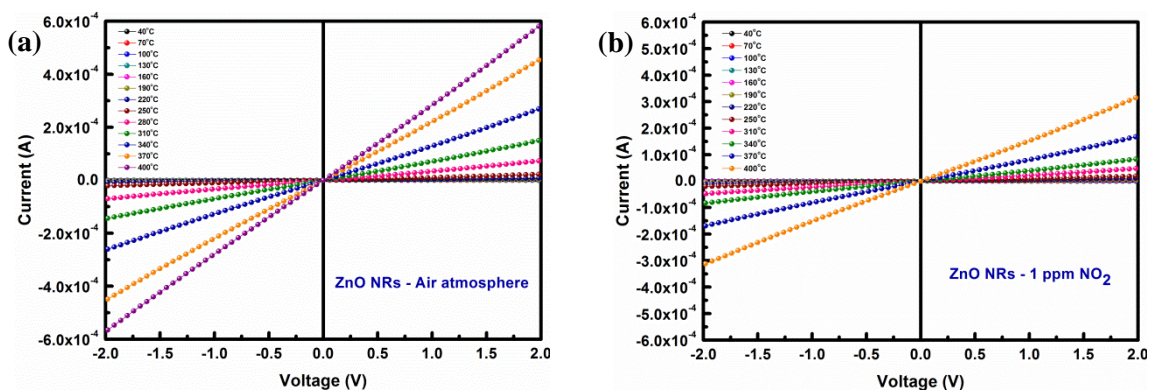


**Figure S5.** (a-b) TEM and HRTEM image images of UL ZnO nanorods and (c) corresponding SAED pattern of ZnO nanorods.

## 6. Electrical Studies:



**Figure S6.** Comparative I-V plots under various environments corresponding to (a) ultra-long ZnO nanorods and (b) ultra-long ZnO@Bi<sub>2</sub>O<sub>3</sub> nanorods.



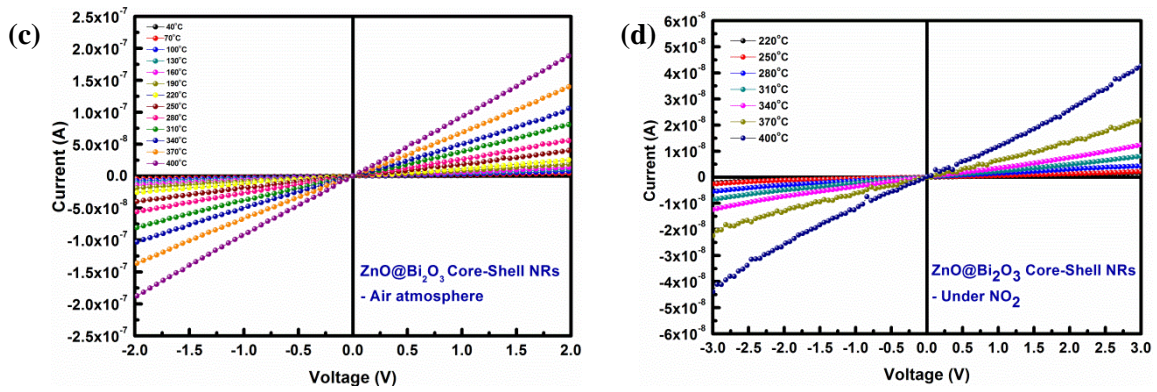


**Figure S7.** Temperature-dependent  $I$ - $V$  characteristics under air and  $\text{NO}_2$  atmospheres (a-b) ultra-long ZnO nanorods (c-d) ultra-long  $\text{ZnO@Bi}_2\text{O}_3$  nanorods.

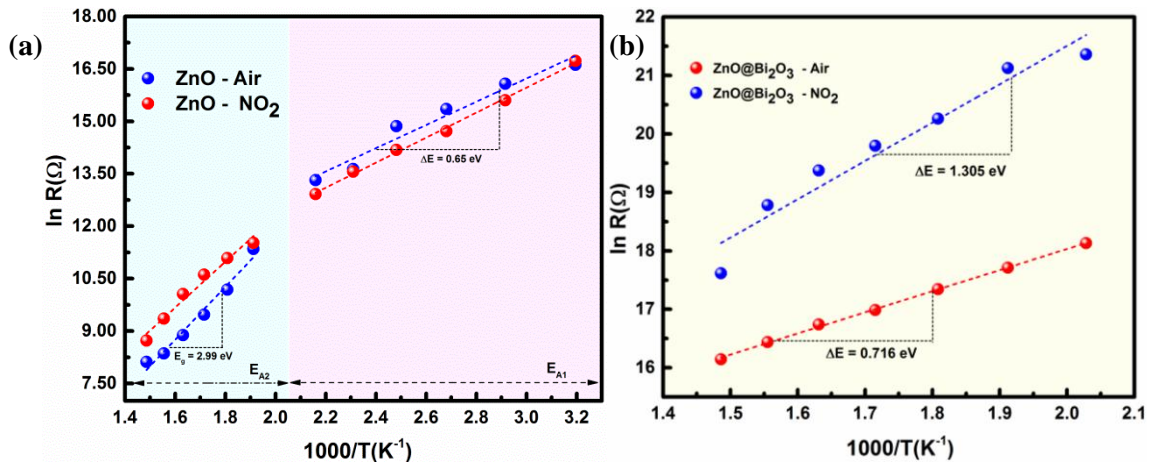


**Figure S8.** Arrhenius plot for ZnO gas sensor under (a) ultra-long ZnO nanorods under air and 1 ppm of  $\text{NO}_2$  and (b)  $\text{ZnO@Bi}_2\text{O}_3$  nanorods under air and 1 ppm of  $\text{NO}_2$  gas environment at  $\pm 3$  V bias.

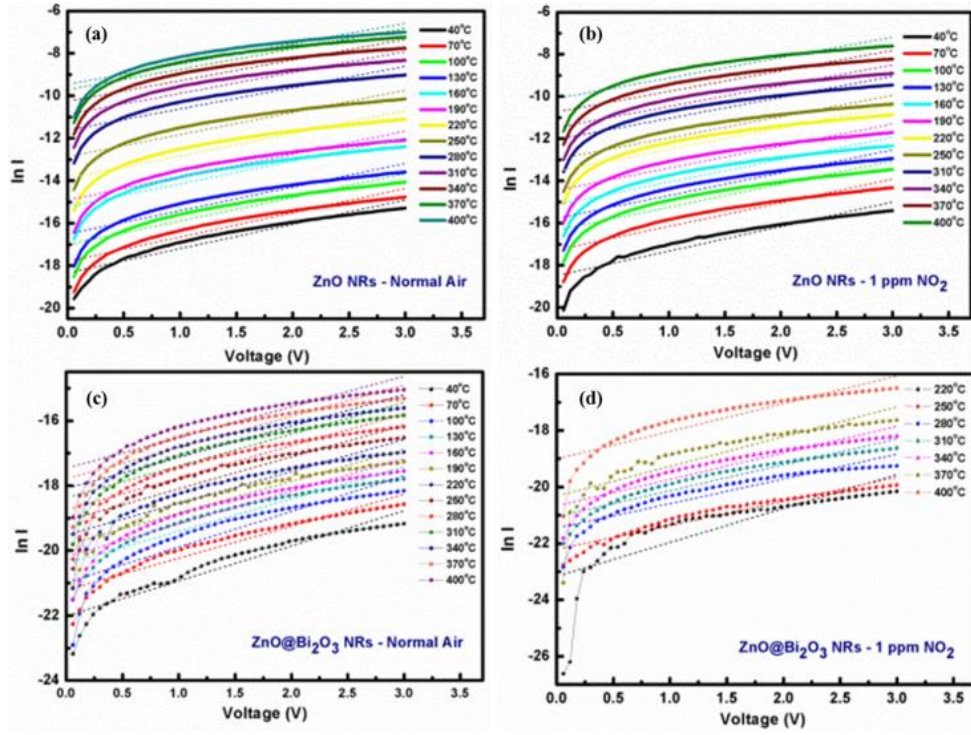


**Figure S9.**  $\ln I$  vs.  $V$  plot under air and 1 ppm  $\text{NO}_2$  exposure of ultra-long ZnO nanorods (a) under air and (b) under 1ppm of  $\text{NO}_2$  and ultra-long  $\text{ZnO@Bi}_2\text{O}_3$  nanorods (c) under air and (d) under 1 ppm of  $\text{NO}_2$ .

The I–V characteristics of a metal-semiconductor contact can be explained based on the thermionic emission theory as per the equation S1,

$$I = A^*T^2 \exp\left(-\frac{q\phi_b}{kT}\right) \exp\left(\frac{qV}{nkT}\right) \quad (\text{S1})$$

Where,  $I_0$  is the saturation current expressed as;

$$I_0 = A^*T^2 \exp\left(-\frac{q\phi_b}{kT}\right) \quad (\text{S2})$$

Where,  $A^*$  is the Richardson constant,  $q$  is the electronic charge,  $k$  is the Boltzmann constant,  $\eta$  is the ideality factor and  $\phi_b$  is the barrier height measured at different temperatures  $T$ .

The value of the Richardson constant  $A^*$  and barrier height  $\phi_b$  were calculated from the Richardson's plot by using the eq.

$$\ln\left(\frac{I}{T^2}\right) = \ln(A^*) - q\left(\frac{\phi_b}{kT}\right) \quad (\text{S3})$$

$$\varphi_b = \frac{kT}{q} \ln \left( \frac{AA^*T^2}{I_0} \right) \quad (\text{S4})$$

Where,  $A^* = \frac{4\pi qm^*k^2}{h^3}$

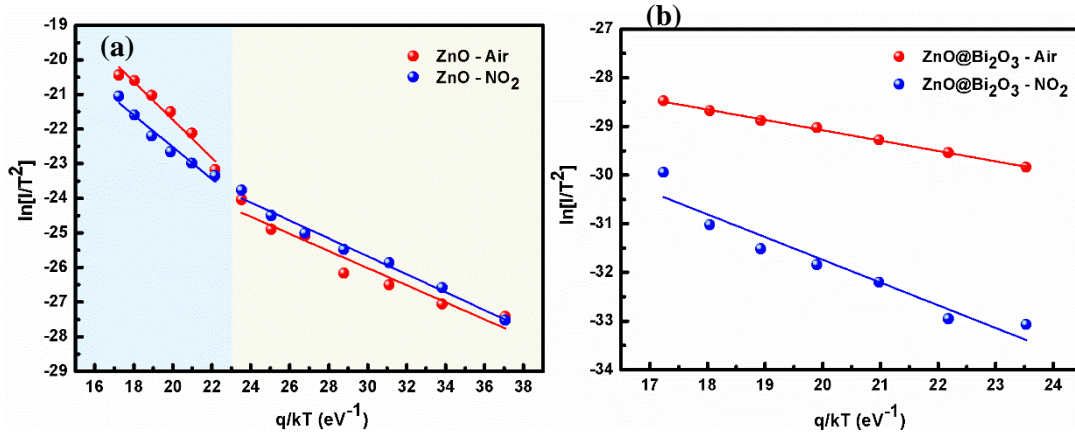


**Figure S10.**  $\ln[I/T^2]$  vs  $q/kT$  plot for ZnO gas sensor under (a) ultra-long ZnO nanorods at air and 1 ppm of NO<sub>2</sub> and (b) ZnO@Bi<sub>2</sub>O<sub>3</sub> nanorods at air and 1 ppm of NO<sub>2</sub> gas environment at  $\pm 2$  V bias.

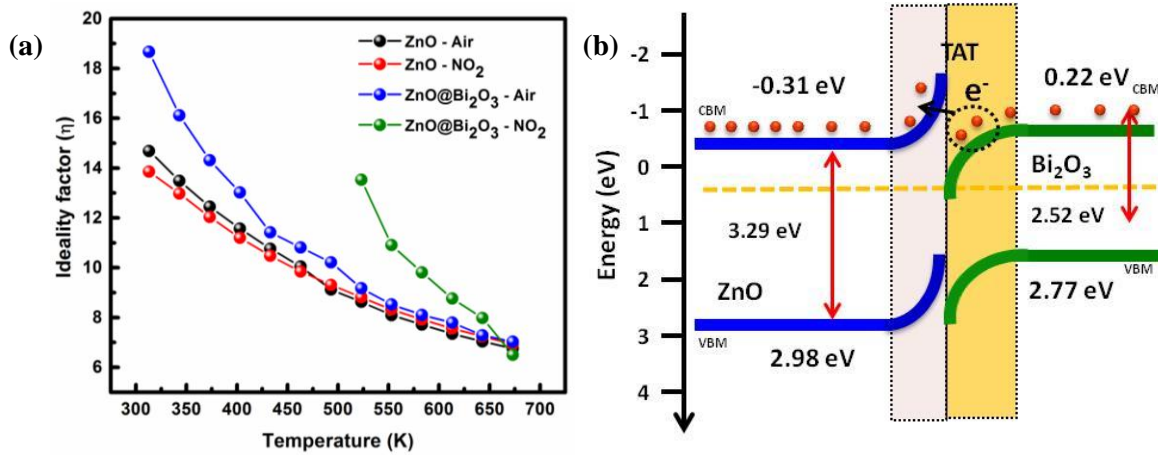


**Figure S11.** (a) Variation of ideality factor as a function of temperature for ZnO nanorods and ZnO@Bi<sub>2</sub>O<sub>3</sub> heterojunction nanorods and (b) Schematic representation of trap assisted tunneling (TAT) in band diagram.

**Table S1.** Experimental results of Richardson Constant and Barrier height.

Sample	Gas Environment	Richardson Constant ( $\text{Acm}^{-2} \text{K}^{-2}$ )	Barrier height (eV)
ZnO NRs	Air	18.6	0.24
	NO <sub>2</sub>	17.8	0.25
ZnO@Bi <sub>2</sub> O <sub>3</sub> NRs	Air	24.8	0.21
	NO <sub>2</sub>	22.4	0.46

**Table S2.** NO<sub>2</sub> Gas sensing parameter of bare and Heterojunction ZnO@Bi<sub>2</sub>O<sub>3</sub> nanorods.

Conc. of NO <sub>2</sub>	Ultra long ZnO nanorods			Heterojunction ZnO@Bi <sub>2</sub> O <sub>3</sub> nanorods		
	Response [(R <sub>g</sub> - R <sub>a</sub> )/R <sub>a</sub> ] S (%)	Response time (s)	Recovery time (s)	Response [(R <sub>g</sub> - R <sub>a</sub> )/R <sub>a</sub> ] S (%)	Response time (s)	Recovery time (s)
0.5	30.79	39	76	306.18	14	71
1	121.97	26	114	651.77	12	80
1.5	186.49	26	196	762.40	11	82
2	290.55	29	166	963.94	10	90
2.5	391.10	35	239	1009.48	10	93
3	498.35	36	256	1518.00	9	104

**Table S3.** Values of constants  $\alpha$  and  $\alpha'$  from Elovich plot.

Conc. of NO <sub>2</sub>	Initial Adsorption rate ( $\alpha$ ) ( $10^{-09}$ ) $\Omega^{-1} \text{s}^{-1}$		Surface Potential barrier ( $\alpha'$ ) M $\Omega$	
	ZnO NRs	ZnO@Bi <sub>2</sub> O <sub>3</sub> NRs	ZnO NRs	ZnO@Bi <sub>2</sub> O <sub>3</sub> NRs
0.5	1.03	-1.31	4.61	1.87
1	3.62	-2.00	8.57	-4.23
1.5	3.08	-3.17	3.29	2.44
2	2.33	-1.09	1.86	1.68
2.5	2.38	-0.669	0.752	1.57
3	2.99	-0.567	1.69	-3.01

## 7. Cross selectivity of the gases:

In order to study the selectivity properties of the heterojunction ZnO@Bi<sub>2</sub>O<sub>3</sub> nanorods towards NO<sub>2</sub> gas, their responses were studied towards exposure to various interfering gases, such as NH<sub>3</sub>, H<sub>2</sub>S, ethanol, acetone, H<sub>2</sub> and SO<sub>2</sub> by keeping the concentration as 2 ppm constant for all gases (Fig. S11). The material was found to be highly selective towards NO<sub>2</sub> compared to other reducing and volatile organic gases due to the presence of Bi<sub>2</sub>O<sub>3</sub> nanoclusters forming heterojunction with ZnO nanorods which enhances the physisorption process. The charge accumulated at the junction interface of Bi<sub>2</sub>O<sub>3</sub> nanoclusters favor the adsorption of the strong oxidizing gas (NO<sub>2</sub>) than other reducing and volatile organic gases.

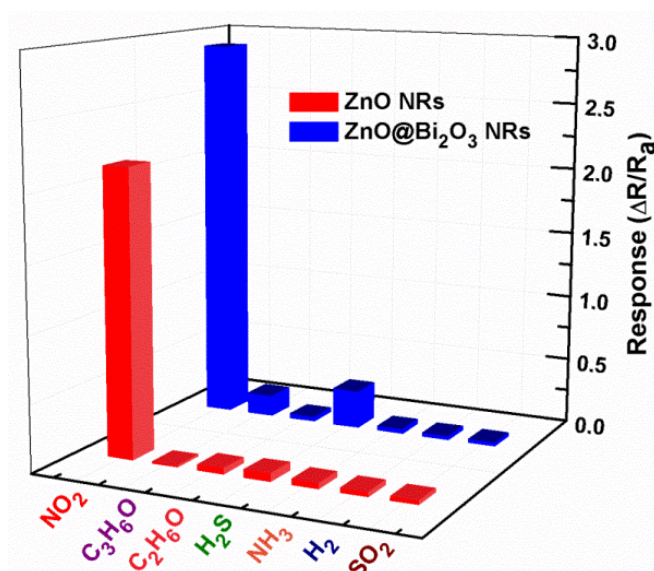


**Figure S12.** Cross selectivity studies of ultra-long ZnO nanorods and heterojunction ZnO@Bi<sub>2</sub>O<sub>3</sub> nanorods

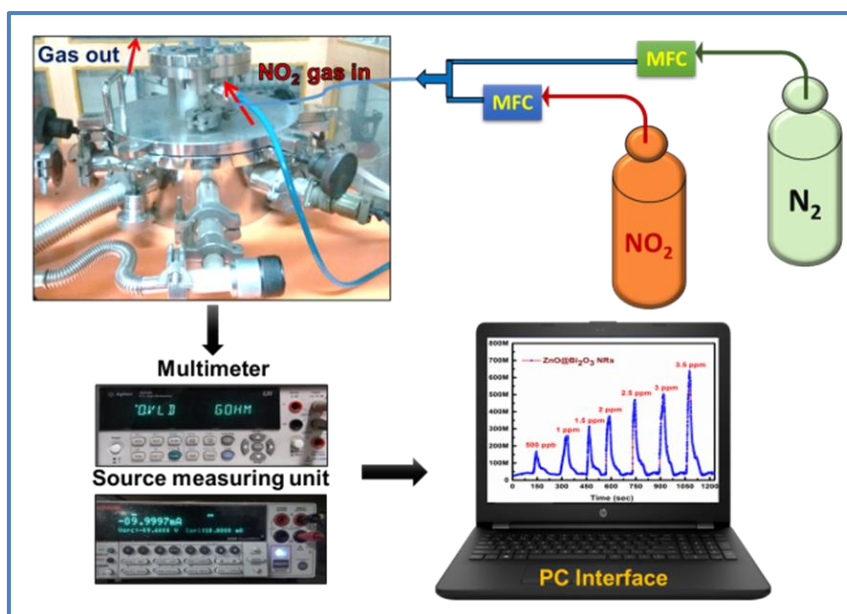


**Figure S13.** Experimental setup used for gas sensing studies of ultra-long ZnO nanorods and heterojunction ZnO@Bi<sub>2</sub>O<sub>3</sub> nanorods.

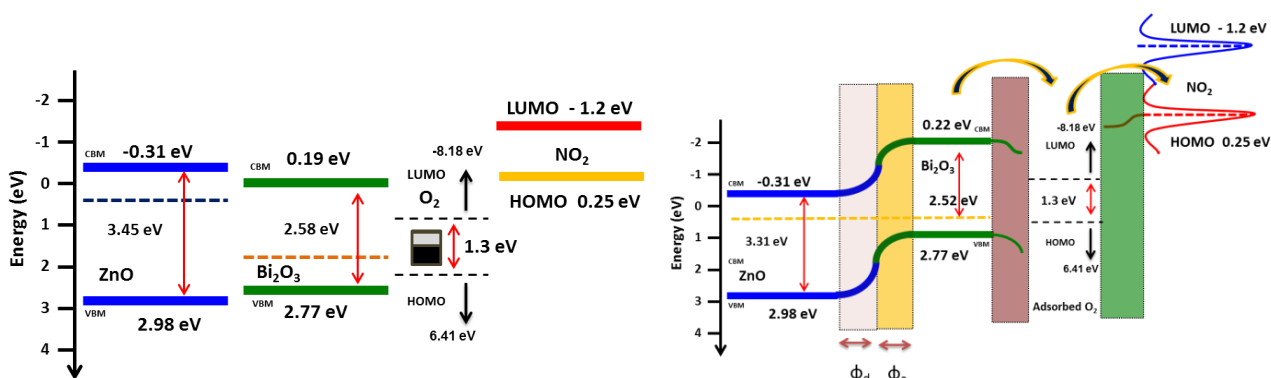


**Figure S14.** (a) Schematic energy band diagrams before forming heterojunction, (b) Schematic energy level diagram of band bending at heterojunction interface during NO<sub>2</sub> exposure.

## 8. N<sub>2</sub> adsorption - desorption analysis:

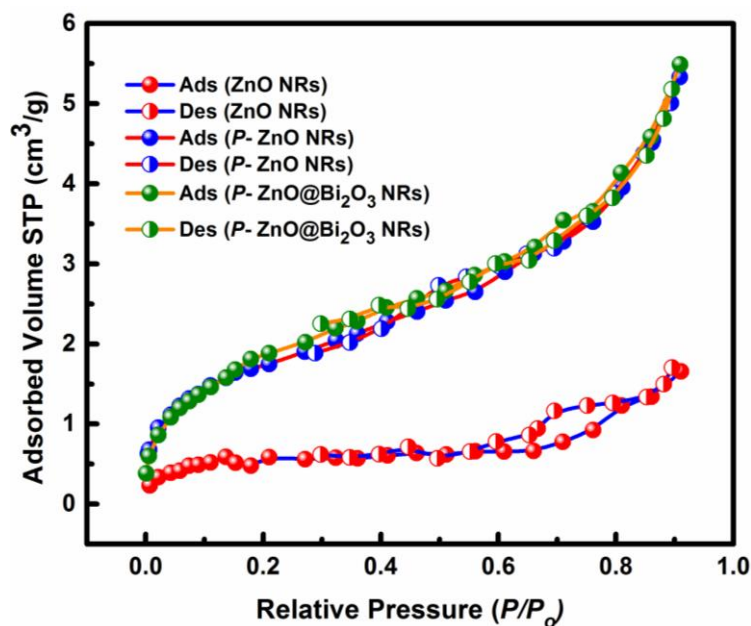


**Figure S15.** Typical nitrogen adsorption–desorption isotherm plots of bare ZnO, porous ZnO and porous ZnO@Bi<sub>2</sub>O<sub>3</sub> nanorods.

The nitrogen adsorption-desorption isotherms of non-porous ZnO, porous ZnO and porous ZnO@Bi<sub>2</sub>O<sub>3</sub> heterojunction nanorods are shown in Figure S15. All materials exhibited typical type IV isotherms with the hysteresis loops at the  $P/P_0$  ranging from 0.1 to 0.9, indicating the existence of the mesoporous structure. The calculated BET surface area of non-porous ZnO, porous ZnO and porous ZnO@Bi<sub>2</sub>O<sub>3</sub> heterojunction nanorods are summarized in Table S4. The BET surface area, pore volume and pore specific surface area of porous ZnO and porous ZnO@Bi<sub>2</sub>O<sub>3</sub> heterojunction nanorods were found to be significantly higher than that of pristine ZnO nanorods. The increase in specific surface area and pore volume can provide abundant surface-active sites and facilitate the easy charge-carrier transport leading to enhanced NO<sub>2</sub> sensing properties.

**Table S4.** BET parameters of Bare ZnO, porous ZnO and porous ZnO@Bi<sub>2</sub>O<sub>3</sub> nanorods:

Sample	Surface area (m <sup>2</sup> /g)	Pore volume (cm <sup>3</sup> /g)	Pore size (nm)	Pore Specific Surface Area (m <sup>2</sup> /g)
Bare UL-ZnO nanorods	1.8816	2.5628	3.0200	3.6655
Porous UL-ZnO nanorods	6.2636	8.2457	3.5133	10.5092
Porous UL-ZnO@Bi <sub>2</sub> O <sub>3</sub> heterojunction nanorods	7.0245	8.4934	3.2405	12.1823

**Table S5.** Comparison of the NO<sub>2</sub> sensing characteristics of *n-p* type metal oxide - based sensors reported in the literature with the present sensor.

Sensor materials	Fabrication method	Measuring range (ppm)	Operating temp.	Response (R <sub>g</sub> /R <sub>a</sub> )	Ref.
<i>n</i> -SnO <sub>2</sub> / <i>p</i> -Cu <sub>2</sub> O Nanofibers	Electrospinning-ALD process	1-10 ppm	300°C	1.21@10ppm	[36]
Bi <sub>2</sub> O <sub>3</sub> -core/ZnO-shell nanobelt	Thermal evaporation-ALD process	1 – 5 ppm	RT	1.98@5ppm	[16]
WO <sub>3</sub> -Bi <sub>2</sub> O <sub>3</sub> Thick films	Screen-printing	5–1000 ppm	350°C	1.78@194 ppm	[37]
<i>p</i> -NiO/ <i>n</i> -SnO <sub>2</sub> Thin films	DC magnetron sputtering	2–10 ppm	200°C	1.44@10 ppm	[38]
<i>n</i> -ZnO/ <i>p</i> -Co <sub>3</sub> O <sub>4</sub> Composite Nanoparticles	Solvothermal method	0.1-5 ppm	RT	7.07@5ppm	[39]
W <sub>18</sub> O <sub>49</sub> /CuO Core-shell nanorods	Sputtering and Thermal Oxidation	0.1-1 ppm	50°C	7.2@1ppm	[40]
CuO NPs-ZnO Nanowires	Thermal Evaporation	1-100 ppm	150°C	1.75@100 ppm	[41]
NiO-In <sub>2</sub> O <sub>3</sub> Composite Nanospheres	Hydrothermal method	0.1 -10 ppm	100°C	17.71@10 ppm	[42]
In <sub>2</sub> O <sub>3</sub> -MoO <sub>3</sub> Nanocomposite	Sol-Gel method	10–200 ppm	500°C	100@100 ppm	[43]
Porous ultra-long ZnO@Bi <sub>2</sub> O <sub>3</sub> Nanorods	Solvothermal method	0.5 – 3 ppm	300°C	15.18@3 ppm	Present work

**References:**

- S. Park, H. Ko, S. Lee, H. Kim and C. Lee, *Thin Solid Films*, 2014, **570**, 298–302.
- B. L. Zhu, C. S. Xie, D. W. Zeng, A. H. Wang and W. L. Song, *Wuji Cailiao Xuebao/Journal Inorg. Mater.*, 2005, **20**, 706–712.
- K. M. S., A. S. Jose, K. Prajwal, P. Chowdhury and H. C. Barshilia, *Sensors Actuators, B Chem.*, 2020, **310**, 127830.
- S. Park, S. Kim, H. Kheel and C. Lee, *Sensors Actuators, B Chem.*, 2016, **222**, 1193–1200.
- Y. Qin, X. Zhang, Y. Liu and W. Xie, *J. Alloys Compd.*, 2016, **673**, 364–371.
- Y. H. Navale, S. T. Navale, F. J. Stadler, N. S. Ramgir and V. B. Patil, *Ceram. Int.*, 2019, **45**, 1513–1522.
- H. Bi, Y. Shen, S. Zhao, P. Zhou, S. Gao, B. Cui, D. Wei, Y. Zhang and K. Wei, *Vacuum*, 2020, **172**, 109086.
- H. Cai, R. Sun, X. Yang, X. Liang, C. Wang, P. Sun, F. Liu, C. Zhao, Y. Sun and G. Lu, *Ceram. Int.*, 2016, **42**, 12503–12507.